**Supporting Information**

**Materials**. FAI was synthesized according to a reported procedure.[1] All the other materials were purchased from commercial sources and used as received.

**Device Fabrication.** FTO-coated glass substrates were patterned by laser scribing and cleaned by ultra-sonication in aqueous washing solution, then rinsed with deionized water, acetone and ethanol. A $TiO_2$ compact layer was then deposited on the substrates by aerosol spray pyrolysis at 450 °C using a titanium diisopropoxide bis(acetylacetonate) solution (75% in 2-propanol, Sigma-Aldrich) in ethanol (1:19, volume ratio) as precursor and oxygen as carrier gas. The mesoporous $TiO_2$ layer composed of 30-nm-sized particles was deposited by spin coating at 5,000 r.p.m. for 20 s using a $TiO_2$ paste diluted in ethanol (1:6, weight ratio). After drying at 125 °C, the $TiO_2$ films were gradually heated to 500 °C, annealed at this temperature for 15 min and cooled to room temperature. The films were sintered at 500 °C for 20 min before use. The 1.0 M perovskite precursor solutions were prepared by dissolving corresponding amounts of CsI, FAI, FABr and $PbI_2$ in DMSO/DMF (1:9 v/v) mixed solvent. The perovskite precursor solution was coated onto the mp-$TiO_2$/bl-$TiO_2$/FTO substrate by a consecutive two-step spin-coating process at 1,000 and 6,000 r.p.m for 10 and 15 s, respectively. At the last stage of spin-coating, 0.1 mL of chlorobenzene was dripped into the film to assist the crystallization and formation of a smooth capping layer. Following spin-coating, the films were annealed on a hotplate at 100 °C for 10 minutes (the $FAPbI_3$ films were annealed at 150 $^{o}$C). After cooling to room temperature, the HTM was deposited by spin coating at 4,000 r.p.m. for 30 s. The HTM solution consists of 72.3 mg (2,29,7,79-tetrakis(N,N-di-p-methoxyphenylamine)-9,9-*spiro*bifluorene)- (*spiro*-OMeTAD), 28.8 μl 4-tert-butylpyridine and 17.5 μl of 520 mg $ml^{-1}$ lithium bis(trifluoromethylsulphonyl)imide acetonitrile solution dissolved in 1 ml chlorobenzene. Finally, 80-nm of gold was thermally evaporated on top of the device to form the back contact.

**Device characterization.** Current-voltage characteristics of the devices were measured with a solar simulator employing a light source and a digital source meter (Keithley Model 2400) using a scan rate of 50 $mV.S^{-1}$. The light source was a 450 W xenon lamp (Oriel) equipped with a Schott K113 Tempax sunlight filter (Praezisions Glas & Optik GmbH) to match the emission spectrum of the lamp with the AM1.5G standard. Before each measurement, the light intensity was calibrated by a Si reference diode equipped with an infrared cut-off filter (KG-3, Schott). IPCE spectra were recorded as a function of wavelength under a constant white light bias of approximately 5 mW $cm^{-2}$ supplied by an array of white light emitting diodes. The excitation beam coming from a 300-W xenon lamp (ILC Technology) was focused through a Gemini-180 double monochromator (Jobin Yvon Ltd) and chopped at approximately 2 Hz. The signal was recorded using a Model SR830 DSP Lock-In Amplifier (Stanford Research Systems). All measurements were conducted using a non-reflective metal aperture of 0.16 $cm^2$ to define the active area of the device and avoid light piping through the sides and the cover glass. For the stability tests, the devices were kept in the dark and new device performances were measured at periodic intervals.

**Materials Characterization:** The perovskite films used for UV-vis spectra, XRD, XPS, SEM and TEM were prepared by spin-coating on mesoporous $TiO_2$ films following the above-mentioned procedure. The powders for the DSC measurement were prepared by scratching the spin-coated film from the glass support (all the films were annealed at 100 $^oC$ for 5 minutes to remove the solvents). The UV-vis spectra were measured with a PerkinElmer Lambda 950 spectrophotometer. Differential scanning calorimetry (DSC) is measured with a DSC 8000 from Perkin Elmer under $N_2$ atmosphere. The XRD patterns were acquired with a Bruker D8 Discover diffractometer in Bragg–Brentano mode, using Cu K α radiation (1.540598 Å) and a Ni β-filter. Spectra were acquired with a linear silicon strip 'Lynx Eye' detector from $2\theta = 10°–60°$ at a scan rate of 2° $min^{-1}$, step width of 0.02° and a source slit width of 1 mm. The morphology of the films was characterized using a high-resolution scanning electron microscope (ZEISS Merlin). The perovskite structures and compositions were examined by a high-resolution transmission electron

microscope (Technai Osiris, FEI), equipped with an Oxford energy-dispersive X-ray (EDS) detector.

**First principles calculations.** Density functional based first principles calculations were performed starting from the experimental α, β and δ phases of $FAPbI_3$ and $CsPbI_3$[2]. The simulation cells of α and δ phases were obtained replicating the corresponding unit cells so as to obtain the same number of stoichiometric units as in the unit cell of β phase, i.e. 12 units. Mixed cation and halide systems were obtained replacing FA with Cs and I with Br, respectively. For each stoichiometry, when allowed by the composition, we considered 10 different possible replacements, starting from the best configuration at the previous, lower Cs or Br content, stoichiometry. The geometry and cell was then fully relaxed. The difference in energy among the 10 configurations per stoichiometry is typically very low, with a maximum deviation of ~ 0.0003 eV per stoichiometric unit, i.e. ~1/100 of the thermal energy, $k_BT$, at room temperature. This justifies an estimate of the mixing entropic contribution to the free energy by the analytical formula for ideal alloys: $T\Delta S=k_BT[x\log x+(1-x)\log(1-x)]$.

Geometry and cell optimization of the various systems was performed using the generalized gradient approximation to density function theory (GGA-DFT) in the Perdew-Burke-Ernzerhof (PBE) formulation[3]. The interaction among valence and, in the case of Pb, semi-valence electrons and core electrons and nuclei is described in terms of Rappe-Rabe-Kaxiras-Joannopoulos pseudopotentials[4]. Kohn-Sham orbitals have been expanded in a plane-wave basis set with an energy cutoff of 40 Ry. The cutoff for the density is set to 280 Ry. The Brillouin zone is sampled with a 4x4x4 shifted Monkhorst-Pack mesh of k-points[5].

The accurate determination of the mixing energy requires an energy alignment among the various systems. In fact, in electronic structure calculations in periodic system there is no unique reference energy. In this article, we use an approach analogous to the one used by Pasquarello and coworkers for band alignment in solids[6].

The band structure of selected systems was computed including spin orbit coupling. It has been previously shown that while this approach results in a too small band gap, it produces correct band dispersion[7]. Since cation and halide mixing can induce structural

distortions, we computed the band structure along the high symmetry directions of the triclinic analogue of the simulation boxes, according to the paths reported in literature[8].

Calculation of the variation of the free energy as a function of stoichiometric composition consisted of several idealized steps. We start from the δ phase. A reference system is considered consisting of a fraction, x, of δ-$FAPbI_3$ and a complementary fraction, 1-x, of δ-$CsPbI_3$. From a thermodynamic point of view, a mixed, single phase, system can be formed if its free energy is lower than that of the weighted sum of the free energy of the two compounds (neglecting interface and surface free energy terms). Here, the variation of the free energy is estimated by the sum of the enthalpic and mixing entropy contribution (see the discussion above about the mixing entropy contribution). For the results discussed in this article, T in the mixing energy formula was set to 300 K. Fig. 5 shows that in the case of the δ phase, cation mixing increases the free energy. Thus, for the system it is energetically more convenient to segregate the δ phase into two separated pure (in terms of cationic composition) domains.

A similar analysis, still taking as a reference the pure δ-$FAPbI_3$ and δ-$CsPbI_3$ phases, is performed for the perovskite α and β phases. For convenience of presentation, we further apply a shifting to the variation of free energy such that this is set equal to zero for the pure α and β $FAPbI_3$. Thus, a negative value of the variation of free energy at a given value of Cs content denotes an improved stability of the mixed cation perovskite system, α and β $Cs_xFA_{1-x}PbI_3$. Fig. 6f shows that the relative stability of the mixed cation perovskite phases over the yellow δ phase improves up to a given amount of Cs content, and then, for further Cs mixing, it worsens. It is because of this improved stability that no phase transition from the δ to α/β phases, and *vice versa* is observed in DSC measurements at the operative temperature.

It is worth remarking that the reduction of free energy with Cs content is achieved in different ways between the α and β phase. In the β phase the enthalpic and entropic contributions to the free energy are of opposite sign, with an enthalpic contribution that is slightly positive, and the entropic contribution more than compensating this penalty. In the case of the α phase, both contributions are negative leading to a greater stabilization of this phase upon mixing with Cs. From the structural point of view, cation mixing

results in the distortion of the $PbI_3$ lattice. This distortion is distinctly higher in the α than in the β phase (Fig. S8), which in the case of pure FA perovskite is of a more regular structure. The fact that a distortion of the lattice leads to stabilization is consistent with the order of stability in methylammonium lead iodide perovskite, in which the structures become more ordered within the series orthorhombic → tetragonal → cubic as the temperature increases. To determine the stabilization induced by halide mixing we used an approach analogous to the one described above.

Concerning carrier mobility, the change of composition does not significantly affect the effective masses of holes and electrons, which remain close to the values of pure $FAPbI_3$ over the experimentally investigated range of Cs content The effective hole mass passes from $m^h_\alpha$=0.087 to 0.094 in going from the pure FA perovskite to a 25% content of Cs for the α phase, and from $m^h_\beta$=0.116 to 0.123 for the β one. Also the effective mass of electrons is not significantly affected by the cationic composition. $m^e_\alpha$ goes from 0.23 α-$FAPbI_3$ to 0.2 in α-$Cs_{0.25}FA_{0.75}PbI_3$, and from 0.146 to 0.166 for the corresponding β phases. Similar to the case of cation mixing, we did not observe any significant change of $m_h$ and $m_e$ associated to halide mixing for the experimentally investigated composition range.

We also performed simulations of the trends in XRD patterns as a function of Cs content. At a Cs fraction of 20% or higher two additional peaks appear in the region 2θ ~ 26° and 28°. The first peak is, indeed, already present in the pure β-FAPbI3 (it is barely visible in the Fig. 2a between the more intense peaks at ~24° and ~27°, the second due to the FTO). At higher Cs content the feature at ~ 26° becomes more intense and reveals to correspond to several peaks associated to different crystallographic planes (see Fig. S11a and b). In pure FA and Cs-poor samples the interplane distance of these planes is the same, and the corresponding peaks are not distinguishable. At high Cs content the lattice distortions make the interplanar distances of the various planes in this angular region different, and the peaks only partly overlap, giving raise to the complex feature at ~26°. The peak at 28° is, indeed, better interpreted as a splitting of the single peak of the original β-$FAPbI_3$ system. At low Cs content, $x < 0.2$, the structure is cubic-like and the Pb-Pb distances along the three Pb-I-Pb directions are the same. At higher content this symmetry is

broken, giving raise to the split peak (see Fig. S11a and c). Consistent with experiments, this splitting increases with higher Cs content. Another tangible effect is that both peaks are shifted toward larger angles. This is due to an overall shrinking of the lattice with the replacement of the larger FA by the smaller Cs.

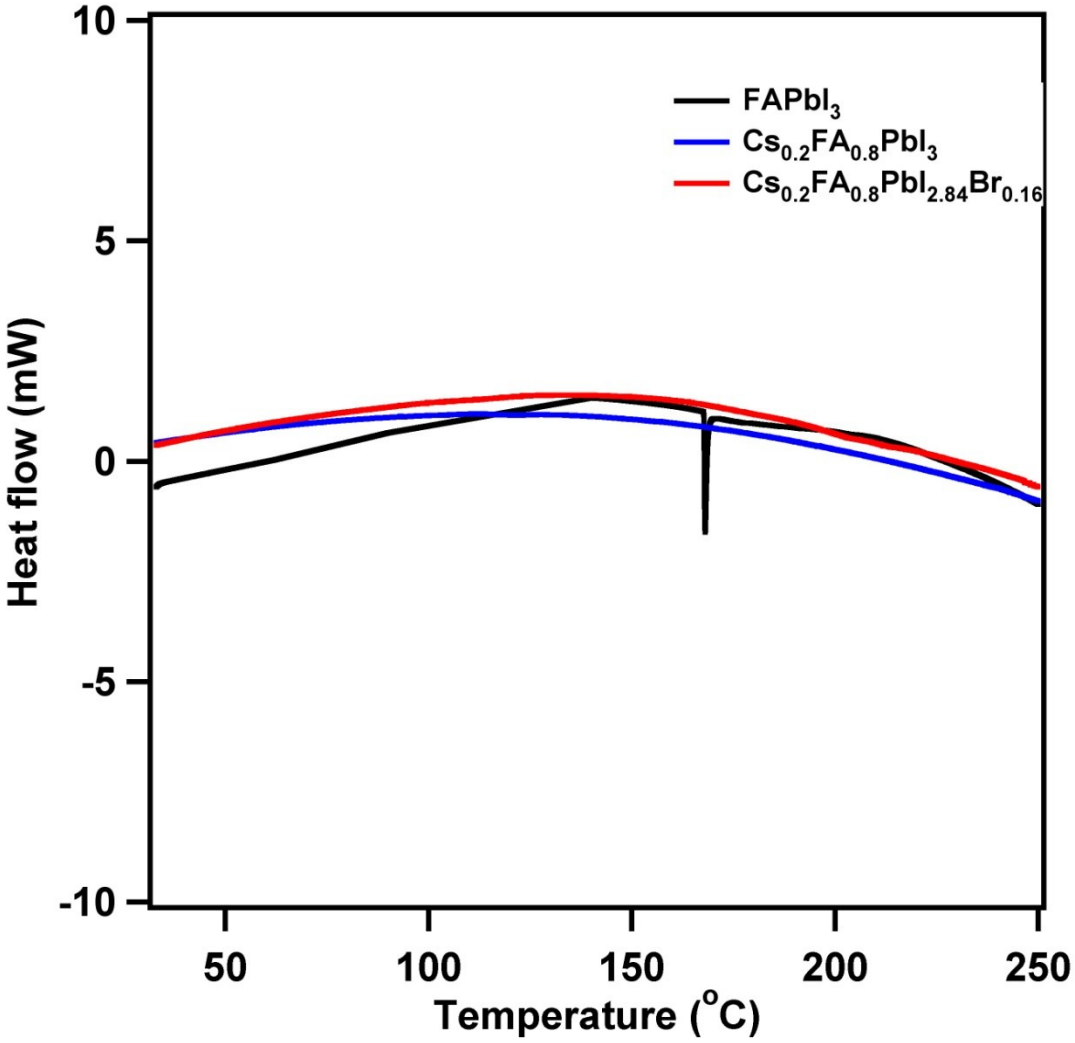


**Fig. S1. DSC of $FAPbI_3$, $Cs_{0.2}FA_{0.8}PbI_3$ and $Cs_{0.2}FA_{0.8}PbI_{2.84}Br_{0.16}$.** The DSC measurements were tested under $N_2$ atmosphere.

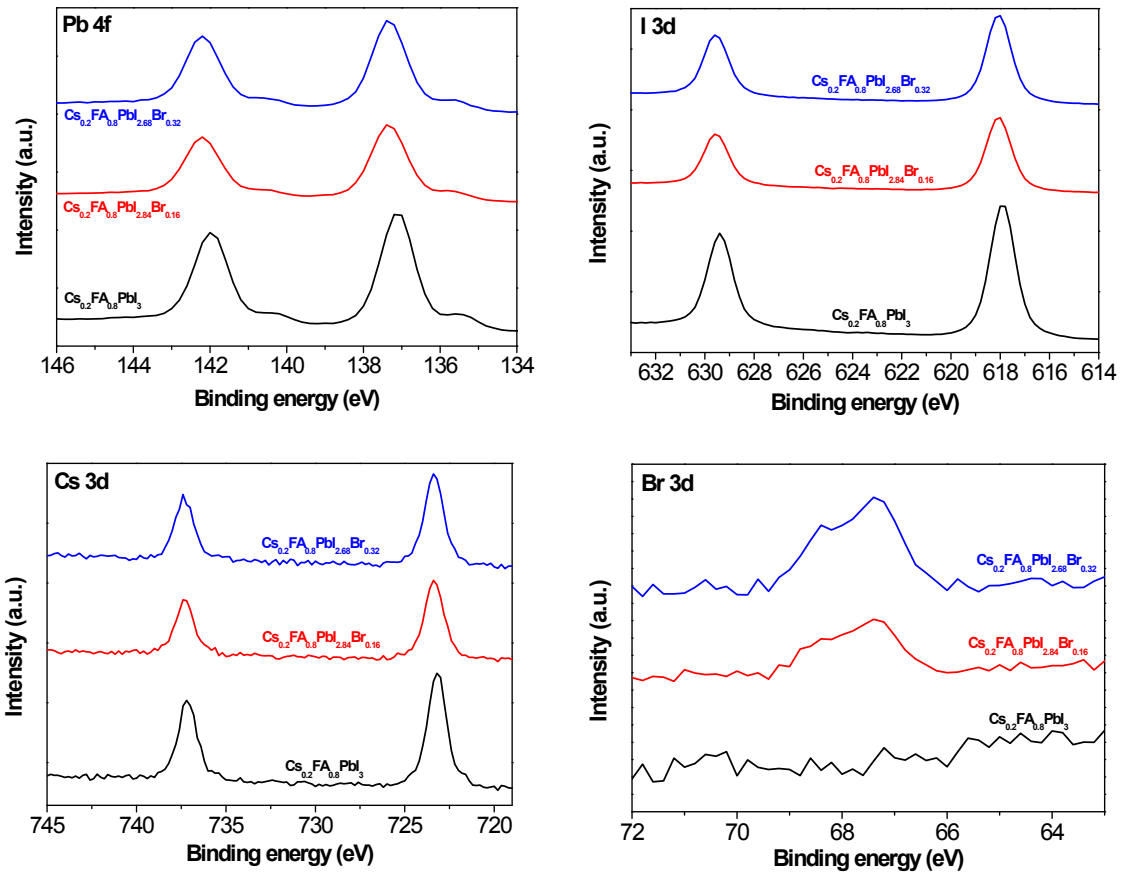


**Fig. S2. XPS spectra of $Cs_{0.2}FA_{0.8}PbI_{(3-y)}Br_y$ perovskite films**

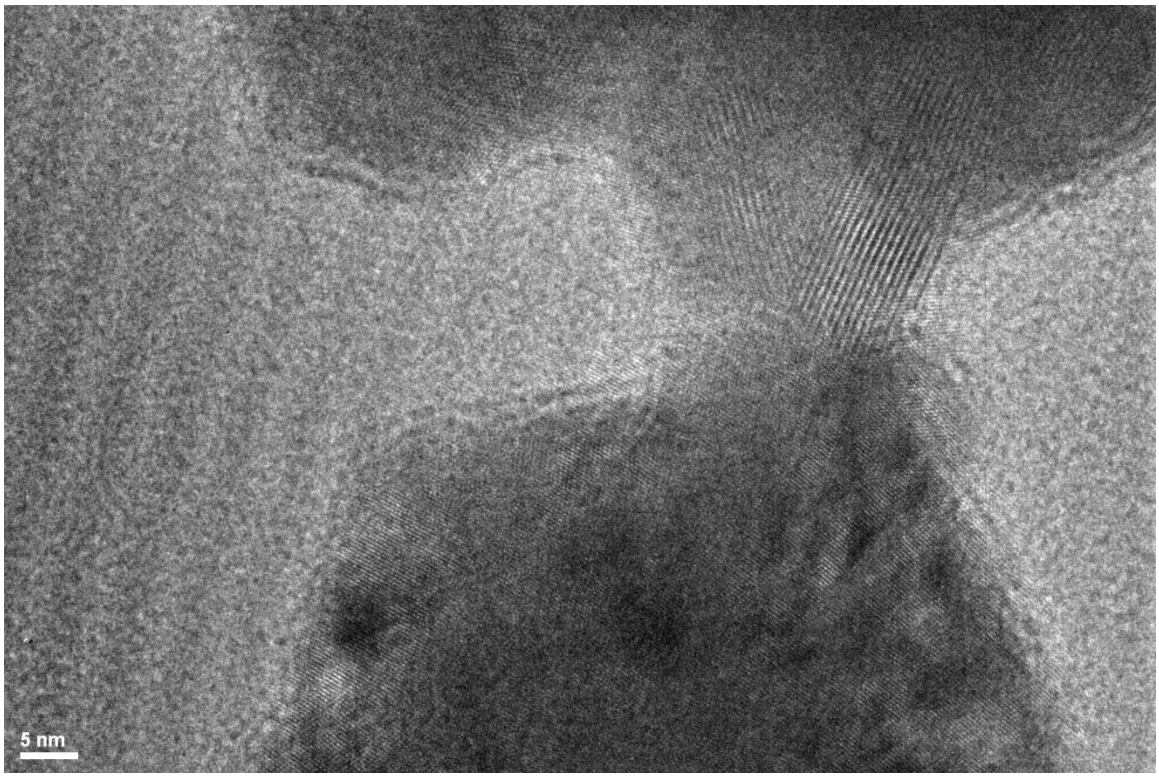


**Fig. S3. High resolution TEM image of the $Cs_{0.2}FA_{0.8}PbI_{2.84}Br_{0.16}$ perovskite.**

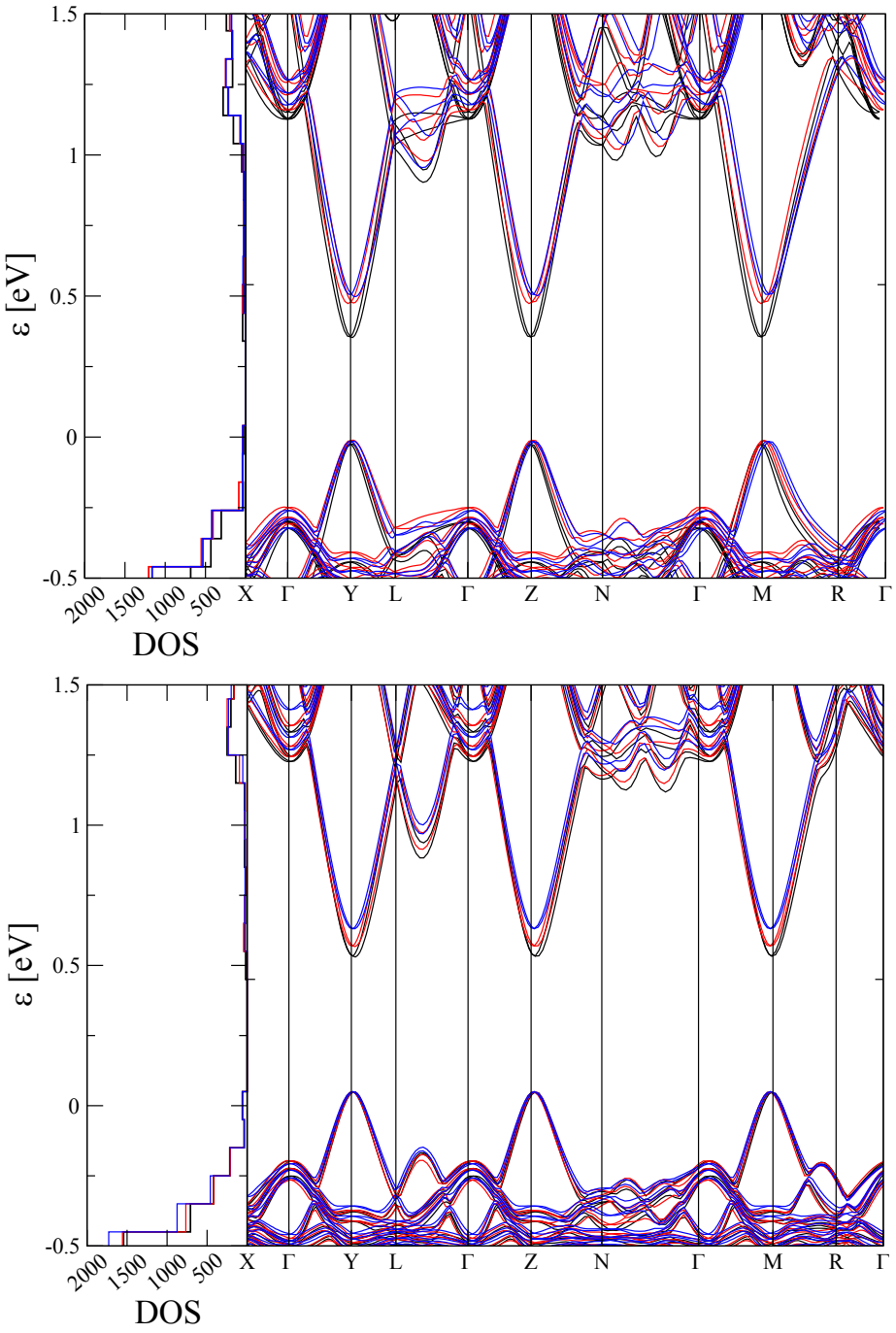


**Fig. S4**: Band structure of the α (top) and β (bottom) phase at $x = 0$ (black), $^{0.08}$ (red) and 0.25 (blue) Cs content. Bands are aligned such that the energy of the VMB is 0. On the left hand of the main panel the density of state (DOS) is shown. This is obtained by

binning the energy range, with bins of 0.1 eV, and building the corresponding histogram of the band structure.

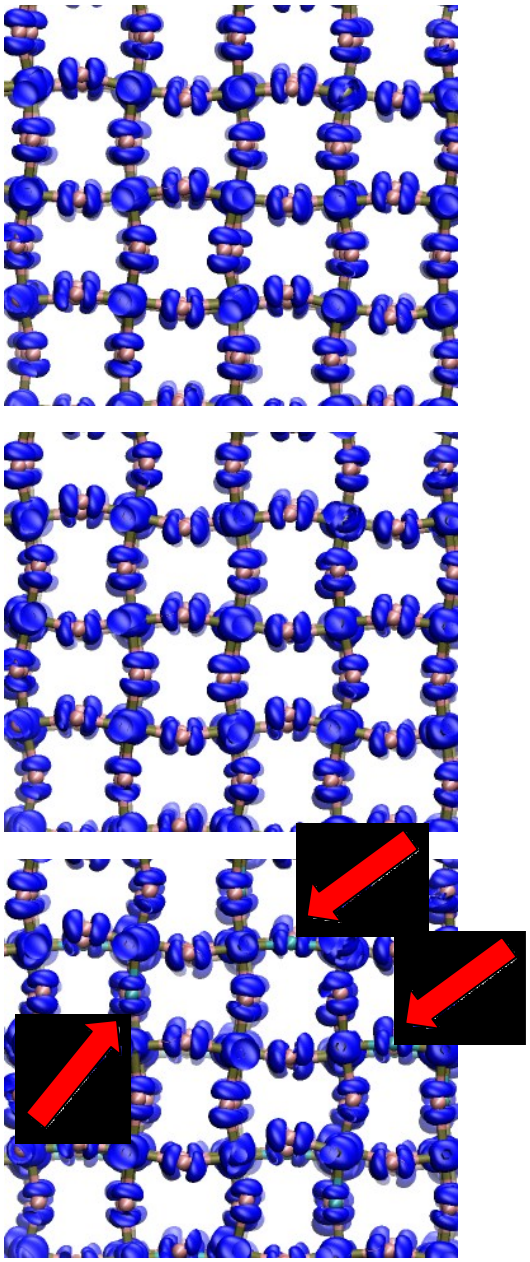

**Fig. S5: Valence Band Maximum (VBM) crystal orbital of (top) $FAPbI_3$ and (middle) $Cs_{0.25}FA_{0.75}PbI_3$ and (bottom) $Cs_{0.25}FA_{0.75}PbI_{2.5}Br_{0.5}$.** For convenience, only Pb (green), I (pink) and Br (cyan) atoms are shown. It can be seen that the decrease of the Pb-I-Pb angle induced by the cation mixing results in a reduction of the antibonding interaction between I-5p and Pb-6s atomic orbitals. Halide mixing further increases the distortion of the structure, with a corresponding reduction of the Pb-6s and and X-p

antibonding overlap. In addition, the more compact Br-4p atomic orbitals (indicated by red arrows) further reduce the antibonding overlap in this crystal orbital.

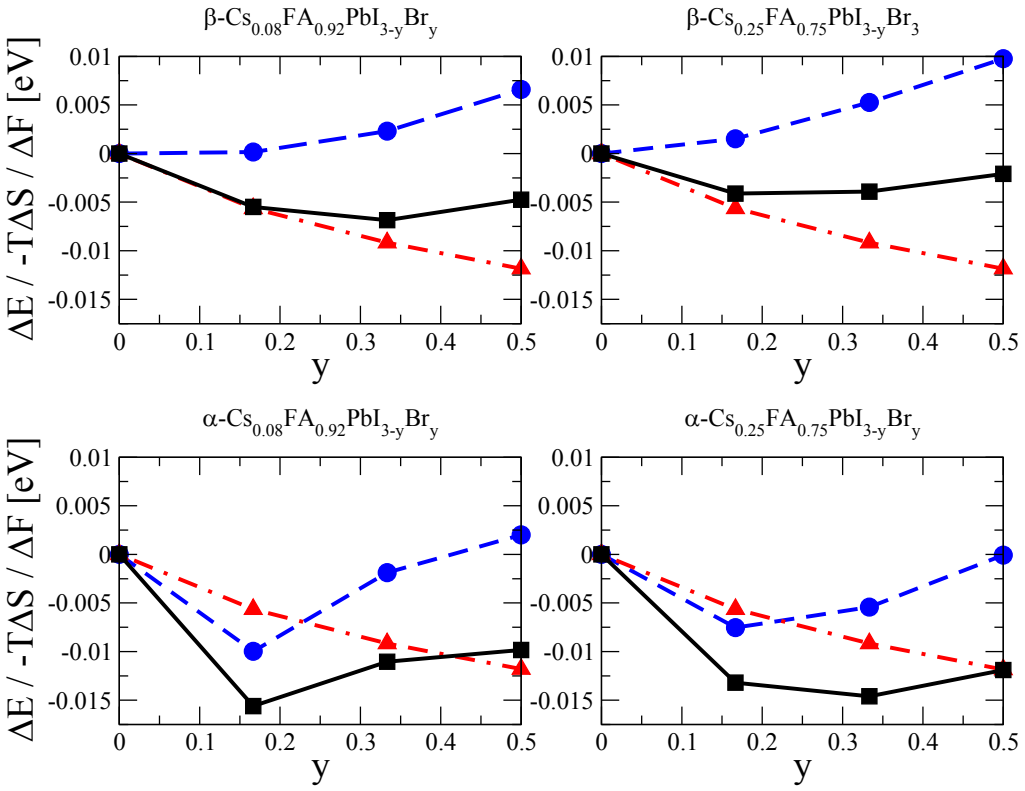


Fig. S6: Variation of internal energy $\Delta E$ (blue), mixing entropy contribution $-T\Delta S$ (red), and free energy $F=\Delta E-T\Delta S$ (black) as a function of Br content y for α and β phase of $Cs_xFA_{1-x}PbI_{3-y}Br_y$ with x=0.08 and 0.25.

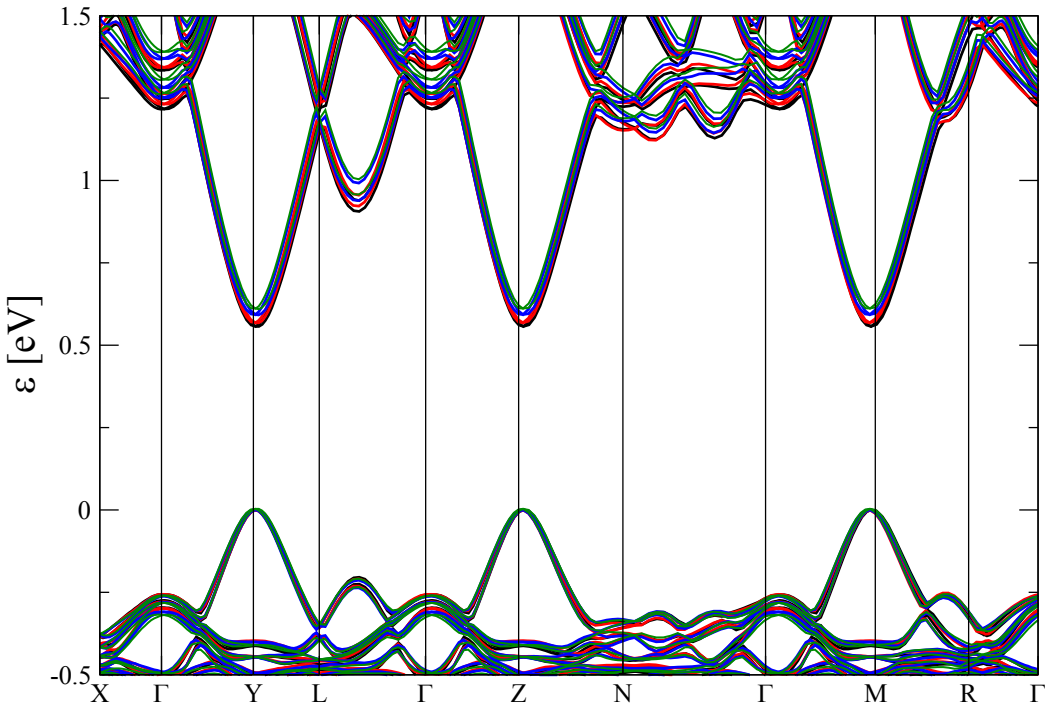


**Fig. S7: Band structure of the $Cs_{0.25}FA_{0.75}PbI_{3-y}Br_y$, for y= 0 (black), 0.17 (red), 0.33 (blue), 0.5 (green).**

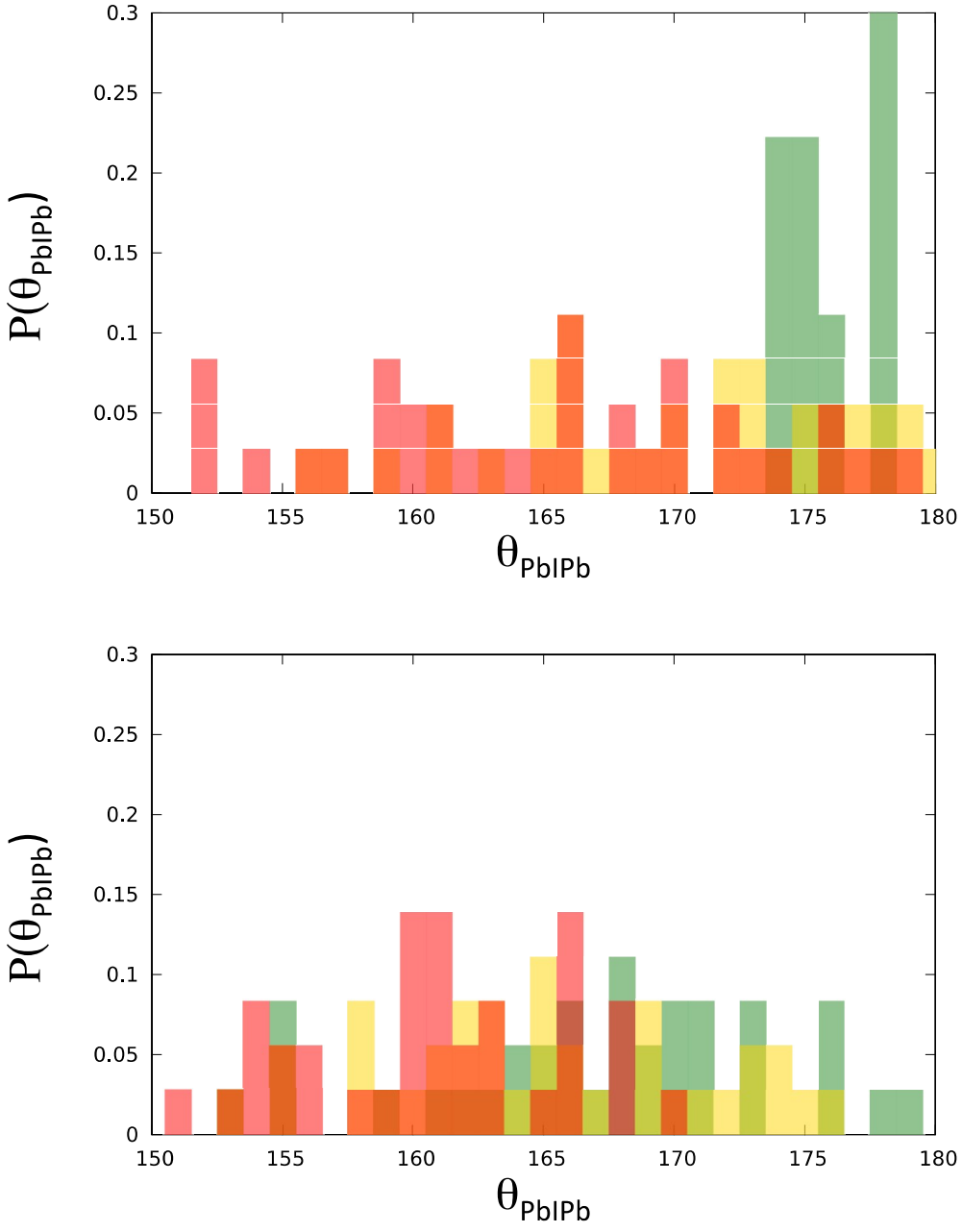


**Fig. S8: Distribution of the Pb-I-Pb angle, $\theta_{PbIPb}$, in $Cs_xFA_{1-x}PbI_3$, with x= 0 (green), 0.17 (yellow), and 0.33 (red).** Data shown in the top panel are relative to the α phase, those in the bottom panel with respect to the β phase. $\theta_{PbIPb}$ in α-$FAPbI_3$ is not 180° because in the calculations the crystallographic sites of this perovskite with fractional occupation must be either occupied or empty, leading to a breaking of the crystal symmetry.

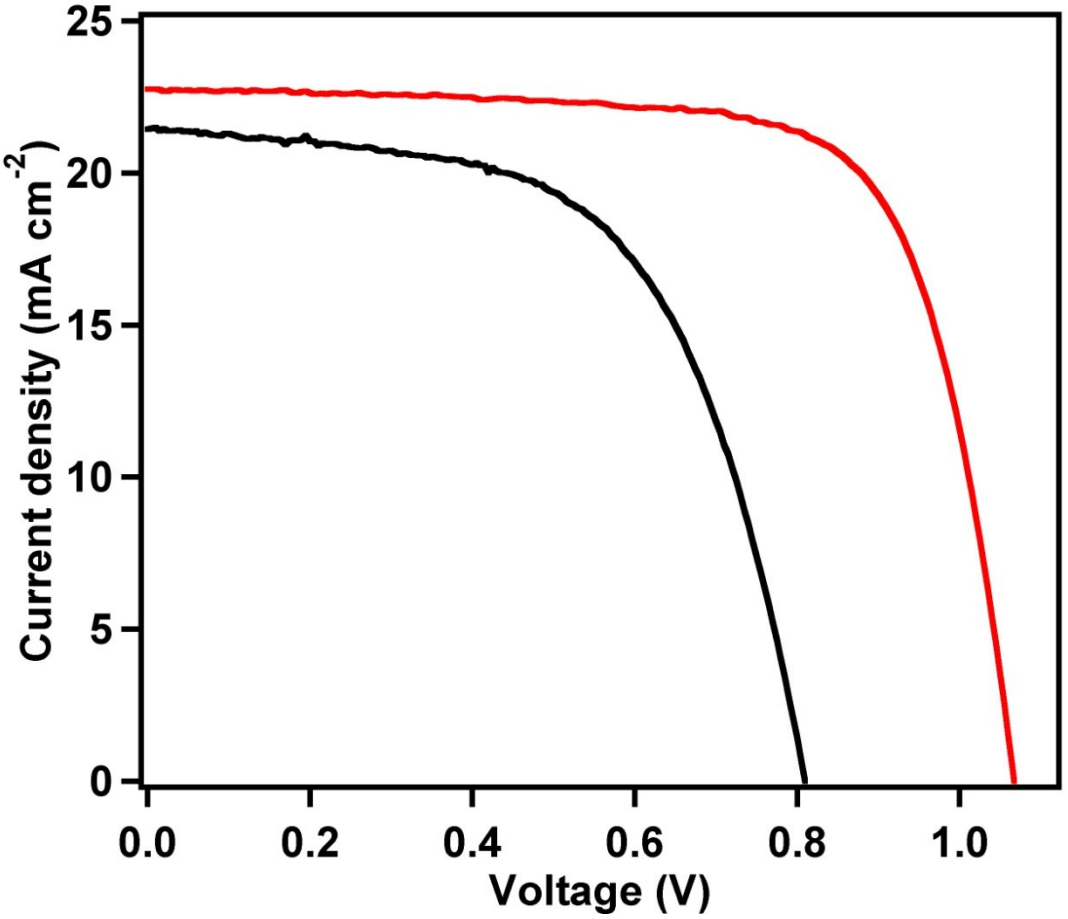


**Fig. S9. J-V curve of the $FAPbI_3$ and champion $Cs_{0.2}FA_{0.8}PbI_{2.84}Br_{0.16}$ perovskite solar cells measured under simulated standard AM 1.5 solar illumination at room temperature.**

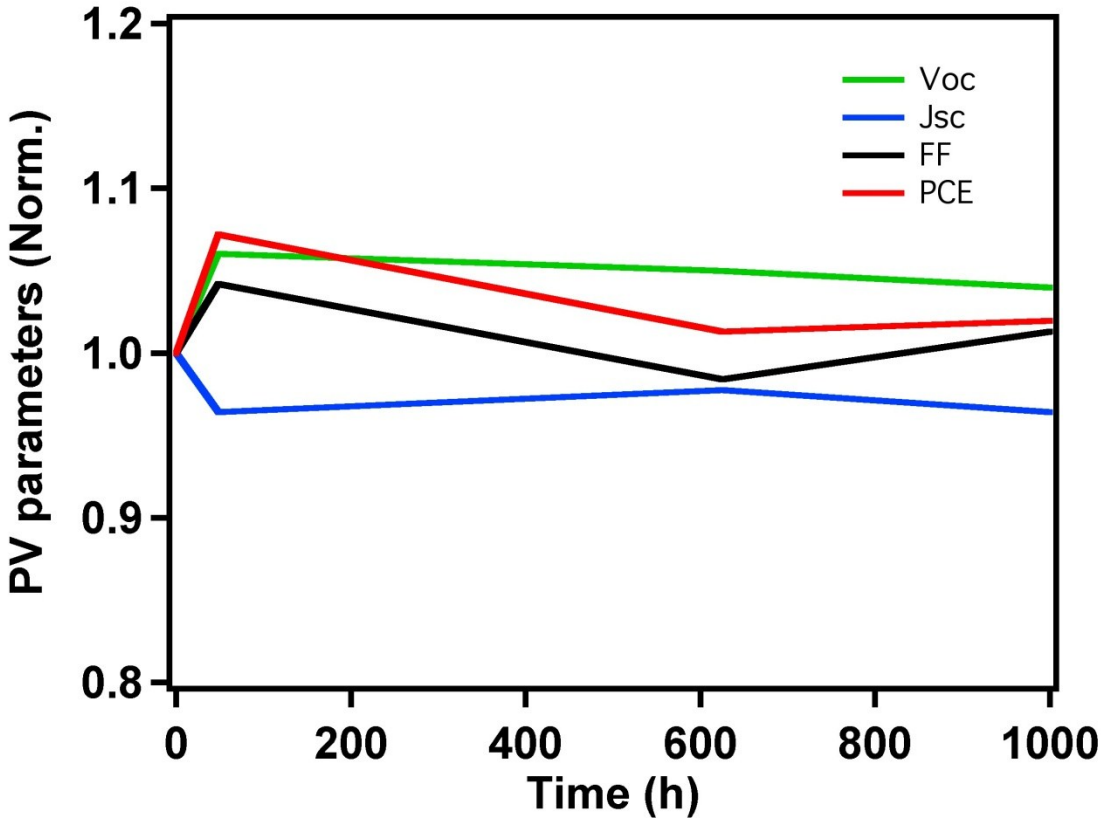


**Fig. S10. Stability test results of $Cs_{0.2}FA_{0.8}PbI_3$.** (ambient conditions in dark)

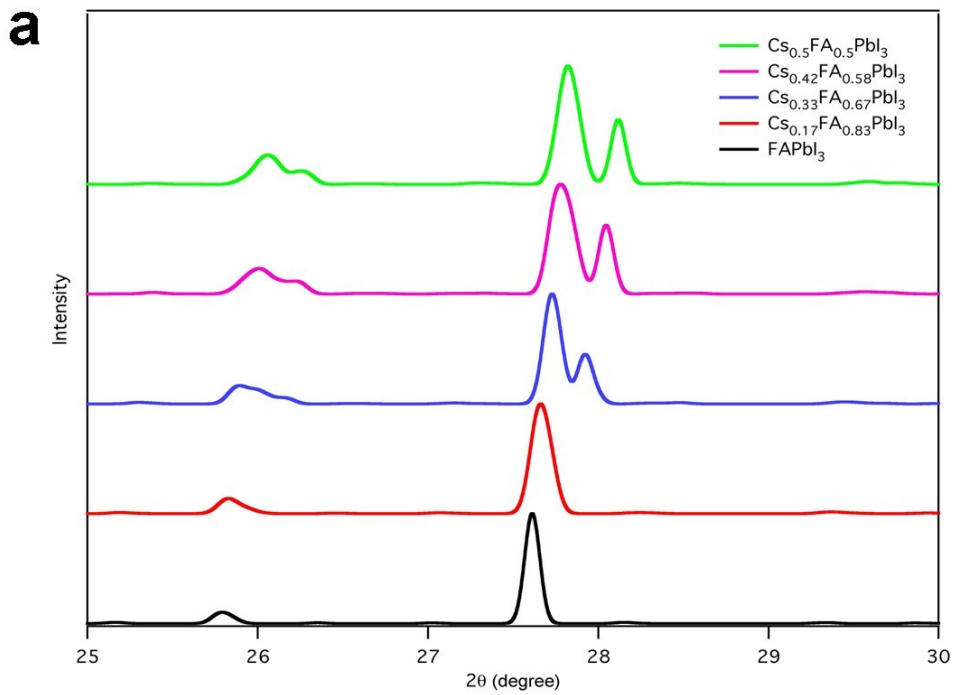
a
Cs0.5FA0.5PbI3
Cs0.42FA0.58PbI3
Cs0.33FA0.67PbI3
Cs0.17FA0.83PbI3
FAPbI3
Intensity
25
26
27
28
29
30
2θ (degree)

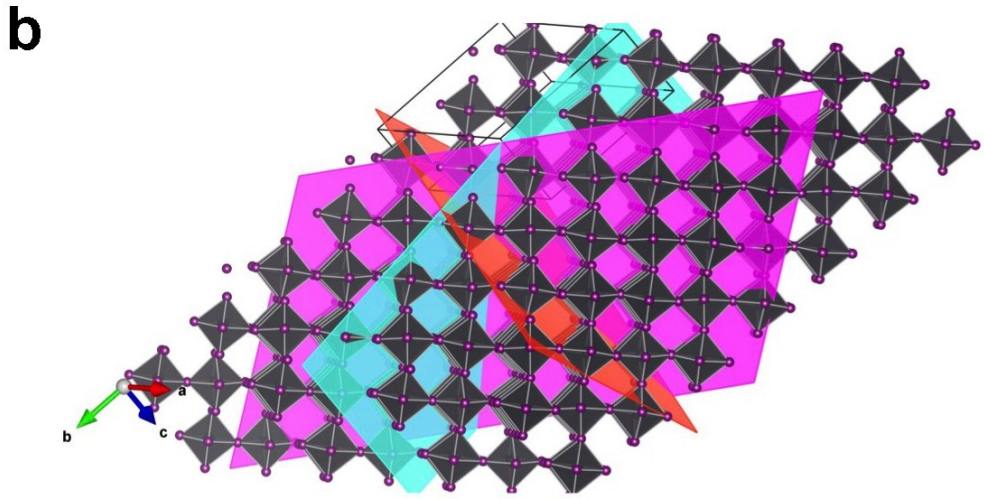
b
a
b
c

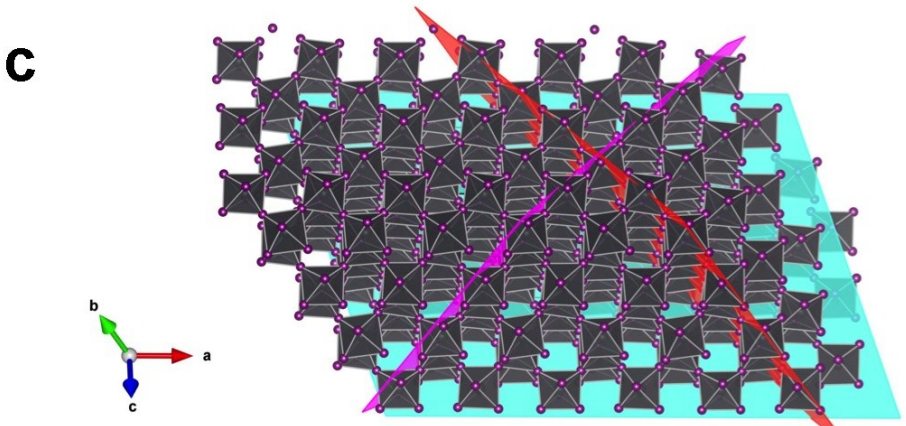
c
b
a
c

**Fig. S11. a** Simulated XRD patterns as a function of composition for Cs content $x$ = 0,0.5. **b** Main crystal planes corresponding to the peak at ~26°: $\bar{3}51$ (red), $13\bar{2}$ (purple) and $5\bar{1}0$ (cyan). **c** Main crystal planes corresponding to the peak at ~28°: $40\bar{2}$ (red), $4\bar{4}2$ (purple) and $042$ (cyan).

**References:**


1. Lee, J. W., Seol, D. J., Cho, A. N. & Park, N. G. High-Efficiency Perovskite Solar Cells Based on the Black Polymorph of HC(NH2)(2)PbI3. *Adv Mater* **26**, 4991-4998 (2014).
2. Stoumpos, C. C., Malliakas, C. D. & Kanatzidis, M. G. Semiconducting Tin and Lead Iodide Perovskites with Organic Cations: Phase Transitions, High Mobilities, and Near-Infrared Photoluminescent Properties. *Inorg Chem* **52**, 9019-9038 (2013).
3. Perdew, J. P., Burke, K. & Ernzerhof, M. Generalized gradient approximation made simple. *Phys Rev Lett* **77**, 3865-3868 (1996).
4. Rappe, A. M., Rabe, K. M., Kaxiras, E. & Joannopoulos, J. D. Optimized Pseudopotentials. *Phys Rev B* **41**, 1227-1230 (1990).
5. Monkhorst, H. J. & Pack, J. D. Special Points for Brillouin-Zone Integrations. *Phys Rev B* **13**, 5188-5192 (1976).
6. Alkauskas, A., Broqvist, P. & Pasquarello, A. Defect energy levels in density functional calculations: Alignment and band gap problem. *Phys Rev Lett* **101**, doi:10.1103/Physrevlett.101.046405 (2008).
7. Umari, P., Mosconi, E. & De Angelis, F. Relativistic GW calculations on CH3NH3PbI3 and CH3NH3SnI3 Perovskites for Solar Cell Applications. *Sci Rep-Uk* **4**, doi:10.1038/Srep04467 (2014).
8. Setyawan, W. & Curtarolo, S. High-throughput electronic band structure calculations: Challenges and tools. *Comp Mater Sci* **49**, 299-312 (2010).